Sol-gel Synthesis of Mn-substituted Copper Ferrite Nano Particles as Anode for Lithium Ion Batteries

Mukhtar Ahmad[1*], Hamid Yaseen[1], Ihsan Ali[2], Komal Rafiq[3*], Shahzada Qamar Hussain[4], Khurram Shehzad[5]

[1] Department of Physics, COMSATS University Islamabad (CUI) Lahore Campus, Lahore 54000, Pakistan
[2] Higher Education Department (H. E. D.), Govt. Graduate College Toba Tek Singh, Govt. of Punjab, Pakistan
[3] Institute of Chemistry, Baghdad-ul-Jadeed Campus, The Islamia University of Bahawalpur, Pakistan
[4] STEM School of Engineering, RMIT University Melbourne, Australia
[5] School of Chemistry and Chemical Engineering, Jiangsu University, Zhenjiang 212013, China

ARTICLE INFO

ABSTRACT

Mn substituted copper ferrites ($Mn_xCu_{1-x}Fe_2O_4$, x = 0, 0.33, 0.67, 1.00) have been synthesized from metal nitrates and citric acid by sol-gel method (chemical process). This study aims to know the effects of Mn substitution on structural, magnetic, and electrochemical properties of copper ferrites. For characterizing the prepared ferrites, different techniques such as X-ray diffraction (XRD), scanning electron microscopy (SEM), and Fourier transform infrared (FTIR) spectroscopy were used. In addition, vibrating sample magnetometer (VSM) is used to investigate the magnetic properties such as saturation magnetization (Ms), residual magnetism (Mr) and coercive force (Hc). A single-phase spinal structure was confirmed by XRD and lattice parameter was increased from 8.36 Å to 8.52 Å with increasing Mn contents. Micrographs of SEM shows that nanoparticles are agglomerated and non-uniform in size. The FTIR analysis shows that theses absorption band about 1422 cm^{-1} to 1434 cm^{-1} was attributed octahedral B-site. For pure copper ferrite, band is shifted towards higher frequency by manganese content. The results from CV showed that the increasing in scan rate and specific capacitance decreases due to increase in the area loop which clearly means that the investigated samples are best for storage devices such as lithium ion batteries (LIBs).

*Corresponding Authors' Email: mukhtarahmad@cuilahore.edu.pk, komalrafiq444@gmail.com

1. Introduction

Energy and environment are two main concerning areas of 21st century. The last few decades have been outrageous as far as the resources for energy and environment is concerned. Certainly, we have been making vibrant blunders in opting for resources to overcome energy requirements. Hence, not only we are facing energy crisis but also serious environment threats which can bring us on the verge of the extinction. The emission of greenhouse such as carbon dioxide (CO_2) have been the major concern to overcome greenhouse effects and gas emission from vehicles (Lain, Brandon, & Kendrick, 2019). As we know the world is fully enriched with abundant energy resources which can come under the orthodox definition of renewable energy. Considering the two fold facts that fossil fuels are limited and their usage causes destructive affects in the environment, naturally there have been lots of attention to promote renewable energy sources. The biggest challenge faced by the renewable energy technology is to find effectual and efficient ways to store energy from these sources. For examples, solar energy is available in generous amount especially in areas which has high solar energy capacity but storage of this energy is a big task. Therefore, energy storage devices technology is being considered a need of modern

era. Batteries has been advanced our time and making remarkable progress, thanks to the physicists and researchers. Out of all the batteries technology lithium-ion batteries have been showing promising potential to overcome energy storage complications due to its good electrochemical properties and delivered energy density of (gravimeter 243 Wh/kg; volumetric 676 Wh/L) (Zhang & Fujimori, 2020). Due to lithium being very light it provides low weight batteries which is of vital importance.

In addition, Lithium-ion technology has strong electrochemical properties and low cyclic fading rate, so lithium is superior to other metals (Blomgren, 2016; Javed et al., 2024). There's a comparison of nickel metal hydride, nickel cadmium and lithium-ion batteries as Energy density (Wh/L) verses Energy density (Wh/kg) (Tarascon, 2010). There's advanced comparison between Lithium-ion batteries and other commercial rechargeable batteries in terms of gravi-metric and volumetric energy. So, lithium-ion batteries have highly advanced as compare to other batteries. The benefits and superiority of lithium-ion batteries towards other batteries (Bruce, Freunberger, Hardwick, & Tarascon, 2012). In contrast, Lithium-ion batteries don't suffer from memory effect problems on nickel cadmium batteries. The voltage of a lithium-ion batteries is 3 time that of typical nickel-based batteries (Castaldi et al., 2021). This shows that lithium-ion batteries are the lightest with high energy density which makes them a very viable solution for future improvements and advancements. Lithium's have many benefits, as well as there are many challenges for lithium-ion batteries have faced. The very first challenge we face is the choice of materials for electrodes and electrolyte. Researchers have been trying many combinations and characterizing those materials to optimize the electrode and electrolytes. Lithium batteries has been showing potential issues, the most common being poor cyclic stability, rapid electrode destruction and shuttle facts due to the dissolution of lithium poly sulfide as end discharge products (Deng et al., 2016; Tang & Hou, 2020). Researchers have been using different neutral doping and induced defects to overcome electrochemical cell problems and improvements in lithium-ion batteries. Moreover, the energy density is mainly governed by the positive electrode of lithium-ion battery, a rough study suggests that by doubling the capacity of electrode, almost 57% of cell energy density can be achieved. Hence the focus of research has been mainly an anode to elevate the electrochemical properties. Therefore, the area of lithium-ion batteries is wide open and hence has research potential to overcome the issues. Consequently, the main objective of my thesis is to introduce electrode material for lithium-ion batteries by characterization and by synthesis of nano-composites.

The need for energy storage devices has been a top priority for researchers and scientists as a means of successfully adapting to renewable energy sources. Lithium is one of the lightest metals and was highly valued by early researchers. However, the first lithium-ion batteries came on the market in 1970 based on work of M. Stanley Whittingham. The achievements awarded through the 2019 Nobel Prize have created a great deal of excitement among scientists in the field of energy storage. The award was jointly presented by John B. Goodenough, M. Stanley Whittingham and Akira Yoshino (Kamat, 2019). The commercial lithium-ion batteries used Ti2S as cathode and lithium metal anode. It shows how lithium ions migrate during charging often called litigation and discharging often called de-litigation moves through the electrode.

Due to the high energy density of lithium metal, there has been a great rebound in the development of secondary batteries, but there are many concerns about using lithium metal as a positive electrode. The first disadvantage was the hazardous problems of the violent chemical reaction of lithium metal at high temperature, which was a factor that needs a lot of attention. Secondly during the recycling process there was an issue of dendrite formation which was another area of concern. Hence soon the researchers shifting towards alternative materials for electrodes and electrolytes. various combinations were tried and researchers decided to move towards nonmetallic electrodes and composites in which the lithium ions are used rather than pure lithium metal, for example Rachid Yazami et al used intercalation of lithium in graphite in 1986 (Kim, Song, Son, Ono, & Qi, 2019).

Lithium-ion batteries come in the technology of energy storage devices, having high energy density due to its light weight and energy density measured in Wh/kg. Ferrites are important because of their various potential applications and interesting physical properties. Copper Ferrites ($CuFe_2O_4$) has attracted much attention due to its long-term application in

various microwave devices and memory core systems (George, Nair, John, Joy, & Anantharaman, 2006). Copper ferrite is one of the most attractive nano-structure materials having equal distribution of tetrahedral and octahedral sites and containing inverse spinel show great properties as an electrode material. $CuFe_2O_4$ and its nano-structure is a good aspirant that exhibits large thermal and chemical stability, shows excellent electrochemical behavior and their application in different fields as energy storage devices.

2. Experimental Details and Characterization Techniques

The sol-gel method is a wet-chemical technique and most popular among the scientists and researchers of various fields. In the last 30 years lots of advanced application have been developed (Dar, Shah, Siddiqui, & Kotnala, 2012; Javed et al., 2024; Martinson et al., 2022; Zeng et al., 2014). This section includes the preparation of manganese doped copper ferrite ($Mn_xCu_{1-x} Fe_2O_4$, x = 0, 0.33, 0.67, 1.00) by the sol-gel method. To prepare the solution of nitrates, 100 ml of distilled water was taken in three different sized beakers for each salt precursor as ($Fe(NO_3)_3.9H_2O$), ($Cu (NO_3)_2$) and citric acid, and stirred them separately on the magnetic stirrer plate until it became homogeneous. For the preparation of all samples, the prepared solution of salts according to the sample's required composition was mixed in another 500 ml beaker to make the Manganese substituted copper ferrites for different compositions and covered with aluminum foil to avoid contamination. To make the 'sol' into 'gel', the solution was heated contentiously on the magnetic hot plate for 2-3 hours at 80-90 ℃ until the gelation process started, and we set its PH to 7 by adding NaOH drop, it's completely evacuated (absorbs the water) at 120-150 ℃ then we left with the ash at 220-250 ℃. Actually, that ash is known as powder. And grinded it to obtain fine powder. Resulting powder was sintered at 500 ℃ for 4 hours in furnace and grinded it again to obtain fine powder.

2.1. Characterization Technique

In this research work, different characterization techniques have been used to study the structural properties, vibration modes, size distribution and electrical & magnetic behavior of synthesized material ($Mn_xCu_{1-x} Fe_2O_4$, x=0, 0.33, 0.67, 1.00). X-ray Diffraction analysis is a technique used in material sciences to determine the crystallographic structure of a material and atomic spacing. Raman is a "spectroscopic" technique typically used to determine the vibrational mode of molecules, although the rotational and other low frequency mode of system may also be observed. Fourier transform infrared spectroscopy (FTIR) is a technique which is used to obtained infrared (IR) spectrum of absorption, emission and photo conductivity of the state of material. VSM is a device for investigating magnetic properties of a sample. The sample is exposed to a uniform magnetic field in order to magnetize. Use to characterize the magnetic properties like D.C magnetization. Cyclic voltammetry is a reliable technique for characterizing the semiconductor materials and devices, based on electrochemical potentiometer apparatus and mostly used in the field of material sciences for the analyzing of charging-discharging phenomenon. The morphology of the material plays an important role in the performance of the material, with this analysis we determines the shape, structure, size, pattern, and roughness of the sample.

3. Results and Discussion
3.1. X-Ray Diffraction Analysis

XRD patterns of the prepared samples of ($Mn_xCu_{1-x} Fe_2O_4$, x=0, 0.33, 0.67, 1.00) sintered at 600 °C for 4 hours are shown in Fig. 1. The structural characteristics of the prepared Copper ferrite material are having cubic inverse spinel structure of the $Mn_xCu_{1-x} Fe_2O_4$ (space group P4132/ (213) confirmed with JCPDS, file no: PDF#49-0266) (Khoso, Haleem, Baig, & Jamal, 2021). There are following reflection planes which are common in all the samples (220), (311), (322), (356), (400), (620), (511) and (440). All planes could be matched and indexed with a face centered cubic (FCC) $Mn_xCu_{1-x} Fe_2O_4$ ferrites. The clearly matching with JCPDS card confirmed the single face of all specimens. The peaks are observed to shift to a higher angles with the increase of Manganese (Mn) content. The

following structural parameters and the impact of substitution of Mn was discussed as follows:

3.1.1. Lattice Constant

The lattice constant (a) is calculated from the inter-planer spacing (d) value by using the relation (1) (Vigneswari & Raji, 2018).

$$a = d \sqrt{h^2 + k^2 + l^2} \tag{1}$$

Here (hkl) known as Miller indices and (d) is the distance between the planes. The lattice constant (a) is increased from 8.37 to 8.53Å (Table 1). This increasing trend is due to the substitution of Mn^{+3} (having ionic radius of 0.65 Å) ions which has a larger ionic radius than the Fe^{+3} (with ionic radius 0.61 Å) ion. This is due to the doping of Mn, cubic structure of $Mn_xCu_{1-x} Fe_2O_4$ (x=0) do not change and Mn was substituted into the crystal lattice.

3.1.2. Crystallite Size (D)

The calculation of the average crystallite size using the Scherrer's formula is given by the formula (2) (Kurmude, Barkule, Raut, Shengule, & Jadhav, 2014).

Table 1
Variation of structural parameters with increasing Mn contents in Copper ferrites

x Content	a (Å)	D (nm)	V (Å3)	Dx (g/cm³)	δ (lines/m²)	ε (1/cm²)
0.0	8.369	20.43	576.544	4.6592	20.87×10^{14}	1.65×10^{-3}
0.33	8.591	18.54	654.659	4.3941	25.70×10^{14}	1.89×10^{-3}
0.67	8.538	14.44	642.551	4.5660	38.94×10^{14}	2.72×10^{-3}
1.00	8.529	10.35	695.225	4.9265	45.56×10^{14}	3.12×10^{-3}

$$D = \frac{0.9\lambda}{\beta\cos\theta} \tag{2}$$

D = Average crystallite size, λ = Wavelength of Cu-Kα radiation (1.5406Å), B = Full width half maxima (311), θ = Bragg's angle, Table 1 shows that the crystallite size increases with increasing the substitution of Mn content. The increment ascribed to larger sized Mn substitution in Cu-ferrites.
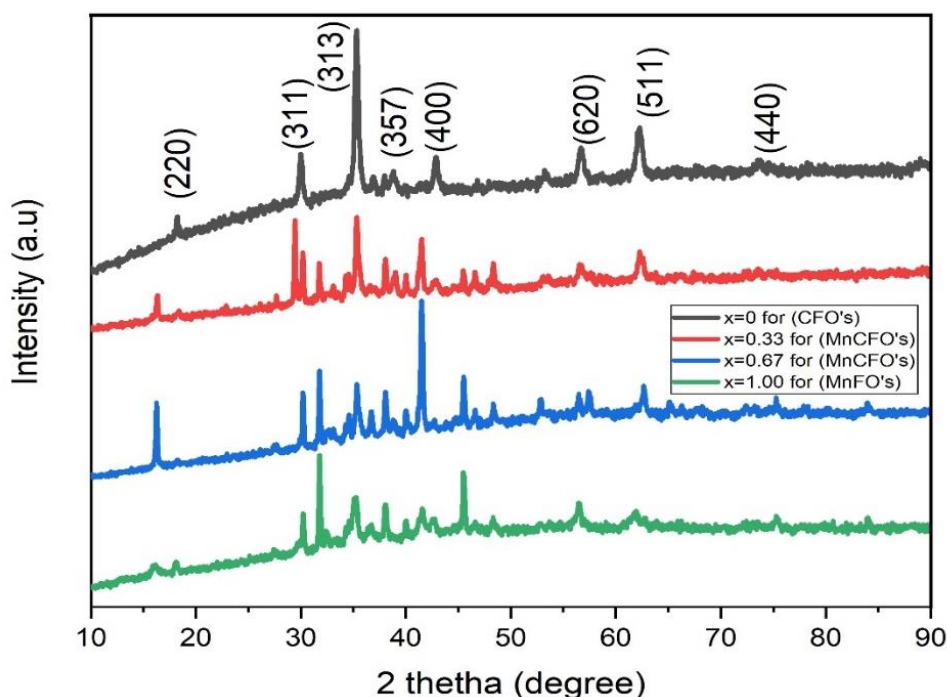

Figure 1: XRD patterns for ($Mn_xCu_{1-x} Fe_2O_4$, x=0, 0.33, 0.67, and 1.00)

3.1.3. Unit Cell Volume (V)

The lattice constant calculated using the volume of the unit cell relationship (3) (Cullity, 1956).

$$V = a^3 \tag{3}$$

As copper ferrite is a cubic shape material having a = b = c, that's why above formula was used to calculate unit cell volume (V). Due to the increasing of lattice parameter, volume of unit cell also increases.

3.1.4. X-Ray Density (Dx)

It informs the density of all atoms or molecules present in the unit cell of the compound. The X-ray density was calculated using the following equation (4) (Kurian & Kunjachan, 2014).

$$D = \frac{8M}{N_A V} \tag{4}$$

Where N_A is known as Avogadro's number (6.022×10^{23}), M = Molar weight, V = Volume of Unit cell. Due to the increasing of lattice parameter, volume of unit cell also increases.

3.1.5. Dislocation Density (δ)

Measured dislocation density is due to the dislocation in unit volume. Dislocation density is determined in lines per unit area and can be calculated using the following formula (Yan & Luo, 2017).

$$\delta = \frac{1}{D^2} \tag{5}$$

Where; D is the Size of crystallite.

3.1.6. Lattice Strain (ε)

The equation 6 used to determine the given parameter and lattice strains was calculated using the given equation (6) (G. Li, 2017).

$$\varepsilon = \frac{\beta}{4\tan\theta} \tag{6}$$

β known as FWHM = full width half maxima, 'θ' is Bragg's angle having (313) plane of maximum intensity.

3.2. Fourier Transforms Infrared Spectroscopy (FTIR)

Infrared spectroscopy is used to find out the current functional groups present in the samples. In spinal ferrite materials, atoms are located in various places called octahedral, tetrahedral sites. The structures are normal and inverted spinals. In the normal spinals, each divalent metal ions are bound to 4-oxide ions, and trivalent metal ions are bound to 6-oxides. As a result, one cell has 8 tetrahedral A sites and 16 octahedral B sites in spinal ferrite cell. The moments of the two sites are opposite, but not equal. Because of spinal minerals are classified as ferrimagnetic materials. In the case of inverse spinal 50% of the trivalent metal ions form octahedral sites and the remaining 50% form tetrahedral sites. Divalent ions of metals form only octahedral sites. As a result, spinals are called a ferrimagnetic material (Reddy et al., 2021). FTIR spectroscopy studies the chemical structure of a material, various types of functional groups, phase composition, and interactions between the chemicals that act in the material. Infrared spectroscopy (IR) of metal ferrites confirmed the behavior of chemical bonds between the given metal ions and other components. The infrared spectrum of the sample is related to the absorbance

associated with organic substances, metal oxides and water molecules. The sintered Cu-ferrites ($Mn_xCu_{1-x} Fe_2O_4$) at 600 ℃ having FTIR spectra has been discussed in the frequency range 4000-500 cm^{-1}.

For first sample that is sintered at 600 ℃. In Fig. 2, the structure and the Fe-O bond length (0.189 nm) of tetrahedral site is smaller than (Cu_2O) octahedral site (0.199 nm). Wavelength and bond length both are inversely proportional to each other that's why in FTIR spectrum peak of octahedral site would appear first with wave number less than that of tetrahedral site. From FTIR, densification of prepared samples is observed (Reddy et al., 2021).

Fig. 2, the Transmission band present in the spectrum at 1422 cm^{-1} is due to the stretching and bending vibration of the C-N=O. Unsintered powder may contain water molecules, nitrate ions and other impurities. IR active molecules with different functional groups at 2491 cm^{-1} preferable to C=C and the absorbance of CO_2 from the air. Therefore, the absorption peak above 3657 cm^{-1} the frequency mode indicating the presence of (OH) hydroxyl group concerned with hydrogen bonded stretching vibration. So the appearance of (3657, 3854) is due to the absorption of water molecules (Akhtar, Ali, Umer, Ahmad, & Khan, 2018; S. Li et al., 2019). Absorption peak at 1422 cm^{-1} appear is due to Fe-O stretching vibration of the octahedron sites. Ferrite bending vibrations is due to Fe-O stretching (S. Li et al., 2019).
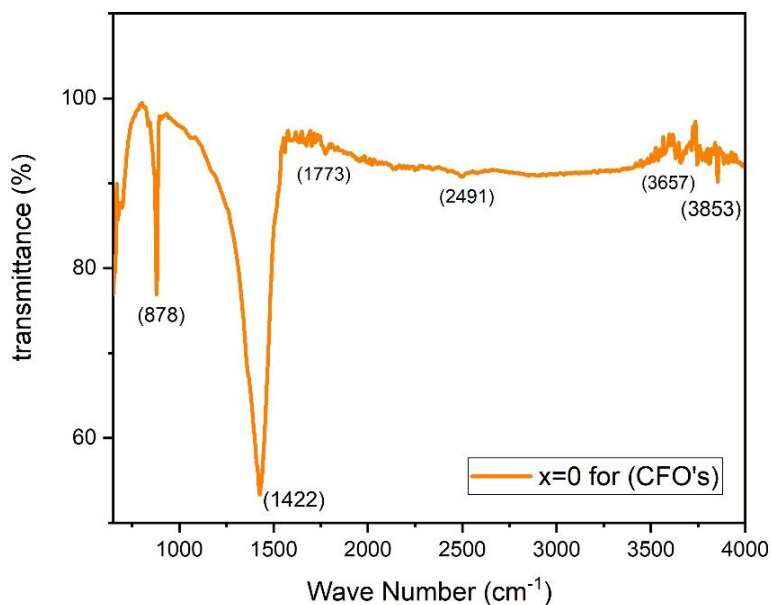

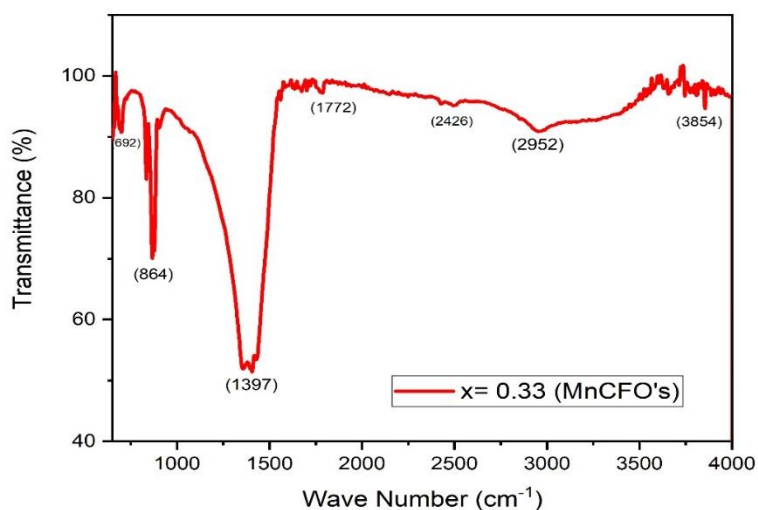**Figure 2: FTIR study for sintered Copper ferrites ($Mn_xCu_{1-x} Fe_2O_4$ at x=0)**

Figure 3: FTIR study for sintered Manganese Copper ferrites ($Mn_xCu_{1-x} Fe_2O_4$ at x=0.33)

Fig. 3 represents the IR spectra of the synthesized $Mn_xCu_{1-x}Fe_2O_4$ having the small substitution of Manganese. A small frequency peak is formed at 1397 cm^{-1}, representing an O-Fe-O group that does not disturb the lithium ferrite structure. The lighter concentration of Manganese change the position of the peaks. Powdered sample $Mn_xCu_{1-x}Fe_2O_4$ at x = 0.33 has absorption peak at 864cm^{-1}, while $Mn_xCu_{1-x}Fe_2O_4$ at x = 0.33 shows absorption peak present at 1397 cm^{-1} is because of stretching vibrations of metal ion at the tetrahedral sites. Peaks appeared at 2952cm^{-1} and 3854 cm^{-1} are because of water molecules present on the surface of the formed sample and the material was stretched (Akhtar et al., 2016).
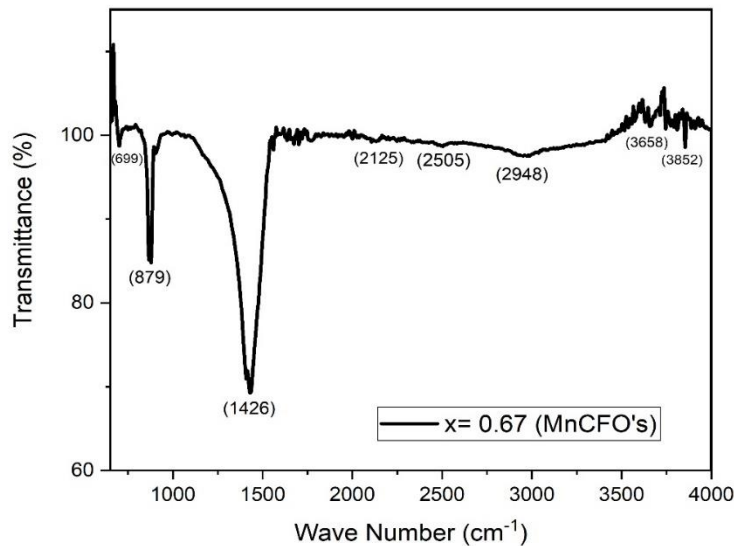

Figure 4: FTIR study for sintered Manganese Copper ferrites ($Mn_xCu_{1-x}Fe_2O_4$ at x=0.67)

Fig. 4, investigate the FTIR spectra of the synthesized ($Mn_xCu_{1-x}Fe_2O_4$ at x=0.67). The same functional groups with the bond strength and structure having octahedral and tetrahedral sites represents in IR spectra. The main band at 1426 cm^{-1} portrayed the crystal lattice vibration. The peak itself at 2948cm^{-1} preferable to C=C nitrate ion adsorbed on the surface of the particles (Akhtar et al., 2016). The peak at 3658cm^{-1} is formed due to the absorbance of water molecule (Anwar et al., 2020). The spectra of ($Mn_xCu_{1-x}Fe_2O_4$ at x=0.50) shows the absorption band fluctuations and shifts during Mn^{+3} ion was introduced. At x=0.50, there is no more shifts or intensity within the band.
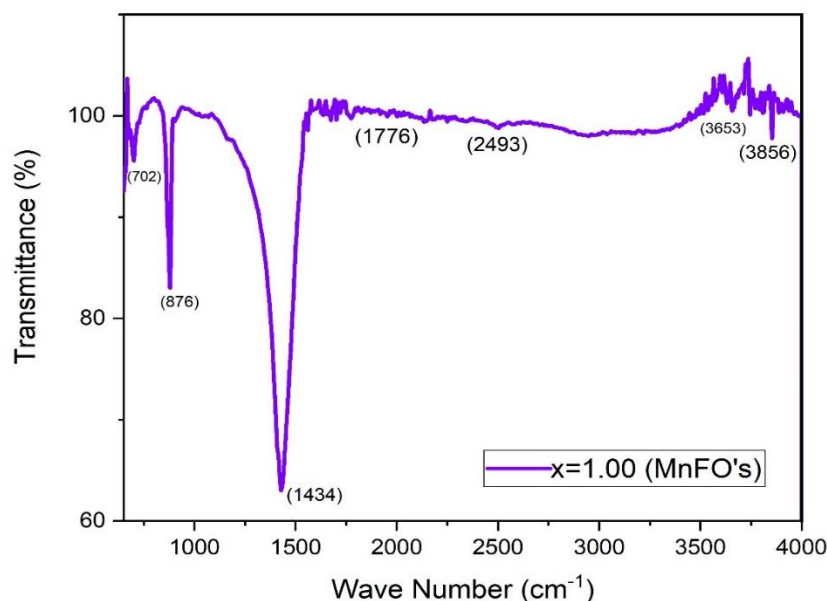

Figure 5: FTIR study for sintered Manganese Copper ferrites ($Mn_xCu_{1-x}Fe_2O_4$ at x=1.00)

Table 2
Values of V_t and K_t for the given samples of Copper ferrites

Contents (x)	V_t (cm^{-1})	$K_t \times 10^5$ dyne/cm
0.00	1422	18.67
0.33	1397	18.02
0.67	1426	18.78
1.00	1434	19.00

Fig. 5, investigate the FTIR spectra of the synthesized ($Mn_xCu_{1-x}Fe_2O_4$ at x=1.00). The same functional groups with the bond strength and structure having octahedral and tetrahedral sites represents in IR spectra. The main band at 1434 cm^{-1} portrayed the crystal lattice vibration. The peak itself at 2493cm^{-1} preferable to C=C nitrate ion adsorbed on the surface of the particles *111.* The peak at 3653cm^{-1} is formed due to the absorbance of water molecule (Anwar et al., 2020). The spectra of ($Mn_xCu_{1-x}Fe_2O_4$ at x=0.50) shows the absorption band fluctuations and shifts during Mn^{+3} ion was introduced. At x=1.00, there is no more shifts or intensity within the band. The stretching vibrations at tetrahedral sites (Vt) was determined from Fig. 3, 4, 5 & 6 and force constants at tetrahedral sites (Kt) was calculated using the following relation (Pachauri et al., 2015; Srivastava, Ojha, Chaubey, Sharma, & Pandey, 2010; Subramanya & Bhat, 2015).

$$K_t = 4\pi^2 Vt^2 C^2 m \tag{7}$$

Where C = speed of light, and 'm' is known as the reduced mass is the Cu^{+2} and O^{-2} ions 'm= 2.60×10^{-23} g', for the octahedral & tetrahedral position. The force constants (Kt) shown in Table 2 are decreased by Mn substitution.

3.3. SEM Analysis

SEM was used and best to analyze the morphological behavior of as-prepared $Mn_xCu_{1-x}Fe_2O_4$ at x = 0, 0.33, 0.67, 1.00 nanoparticles. As typical SEM images depicted in Fig. 6. The obtained SEM images after heat treatment at 600 °C for 4 hours are shown below. Parameter such as grain size was calculated. The micro-graph shows agglomeration within the particles. SEM images spacing is very small so it shows that the adhesiveness of the substituted material is good. The agglomeration part is homogeneous in nature. Increasing in agglomeration by replacing Manganese in Copper ferrite confirmed that Mn is best for the grain growth inhibitor for Copper ferrite nano-particles. Particle size follows the trend of crystallite size, but with the different magnitude. In addition, micro-graphs of sample shows well established having single phase of spinal ferrites. And single-phase shapes are the excellent accepted shapes for microwave absorption usage. Grain size measured by using line intercept method (Thorvaldsen, 1997). For pure Copper ferrites, mean size of grains was 221 nm (Ahmad et al., 2022). The extreme and least diameter of grain was 184.2 nm and 96.5 nm. And Mn substituted copper ferrites that as shown having 286 nm, 324 nm & 373 nm, average grain size (Ahmed, Okasha, Oaf, & Kershi, 2007).

3.4. Magnetic Properties

Magnetic properties of Copper ferrites is shown in Fig. 7. Used ferrites is heated at 600 °C for interval of 4 hours, by changing the temperature of material it effects the saturation magnetization. With the increase in temperature, saturation magnetization (Ms) is decreased, this may be due to the different factors such as surface effect and vitalization of lithium & oxygen. Table 3 depicted the coercivity from the hysteresis loop has few hundreds in oersted values so the prepared lithium ferrites is a soft magnetic material. The prepared material is best for manufacturing of microwave and storage devices. In M-H loop, applied field is up to 10000 Oe for prepared lithium ferrites is shown in Fig. **7**. Different magnetic parameters have calculated from M-H loop of prepared samples such as Coercive force, Magnetization, Magnetic moment, and Ratio of (Mr/Ms) is known as squareness ratio, and Retentivity. The loop is behaving as a ferromagnetic material so it shows lowered movement in saturation magnetization, and net magnetic moment. Due to the exchange interaction between the tetrahedron and the Octahedron site of metal cation, net magnetic moment arises. The change in the interactions from strong Fe^{+3} A-site O^{+2} -Fe^{+3} at B-site to weak Mn^{+3} A-site-O^{+2} -Fe^{+3} at B- site coupling which cause decrease in saturation magnetization (Waldron, 1955).
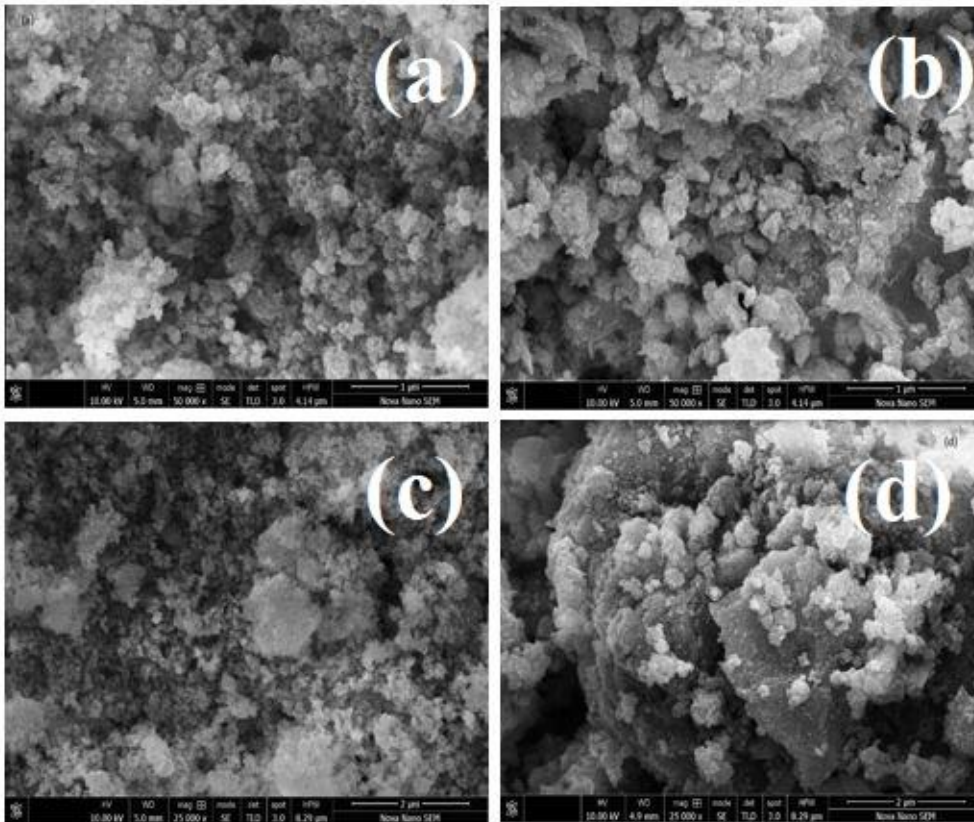
Figure 6: SEM images for $Mn_xCu_{1-x}Fe_2O_4$, (a) x= 0.0 (b) x=0.33 (c) x=0.67 (d) x=1.00

Table 3
Saturation magnetization (M_s), Remanence (M_r), squareness ratio and coercivity (H_c) for all Ce-substituted Li-ferrites

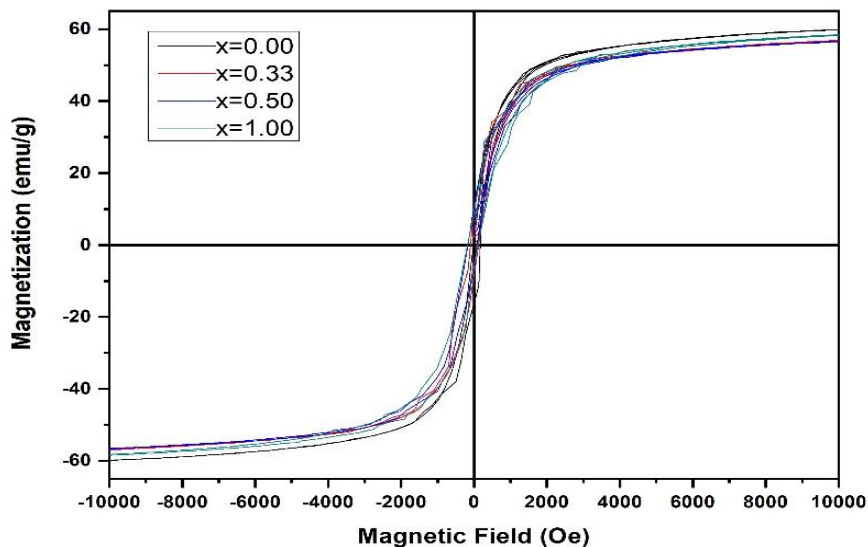| x	M_s (emu/g)	M_r (emu/g)	M_r/M_s	H_c (Oe)
0.00	59.96	7.83	0.13	175.12
0.33	56.97	9.92	0.17	125.76
0.67	55.96	10.87	0.19	82.96
1.00	58.50	9.22	0.15	106.27

Figure 7: *M-H* Loop for Copper Ferrites ($Mn_xCu_{1-x}Fe_2O_4$ at x=0.00, 0.33, 0.50, and 1.00)

3.5. Cyclic Voltammetry (C-V)

Cyclic voltammetry measurements are used to test the electrochemical performance of synthesized samples and were approved out from at different scan rates, 3 mvs , 5 mvs , 10 mvs, 20 mvs , 30 mvs , 40 mvs and 50 mvs in the range of 0.0 to 0.6 for x=0.50 in Hg/HgO electrolyte and $Mn_xCu_{1-x} Fe_2O_4$ as electrode material. Higher and lower peaks in the Fig. 8, represent the reduction and oxidation behaviour which validates the electrochemical performance of synthetic samples. C.V measurements show the increasing behavior of the current and scan rate. When the current is increased by increasing the scan rate so both factors are directly proportional to each other. Literature survey showed that the charge capacity is direct relation with the porosity of the samples which clearly means that used material is best for storage devices. The cathodic reduction of iron ions, it changes from Fe^{+3} toFe^0. Curves in CV spectra show that noise increases with increase in scan rate. The red-ox reaction are given below (Vigneswari & Raji, 2018).

3.5.1. Cathodic Reduction Reaction (CRR)

Complete oxidation reaction is shown as: $2Cu_{0.5}Fe_{0.5}O_4 + 15Cu^+ + 15e^- \rightarrow 5Fe^0 + 8Cu_2O$

3.5.2. Anodic Oxidation Reaction (AOR)

Afterward the cycle, the cyclic voltammetry curve is relax for Copper ferrite nano-particles, which shows the relaxation or stability of the electrode during reduction and oxidation process. The area noted under the curve in the V-I graph depicts the high rating power of battery. Complete reduction reaction (CRR) is noted as below (Lim, Teoh, Liew, & Ramesh, 2014).
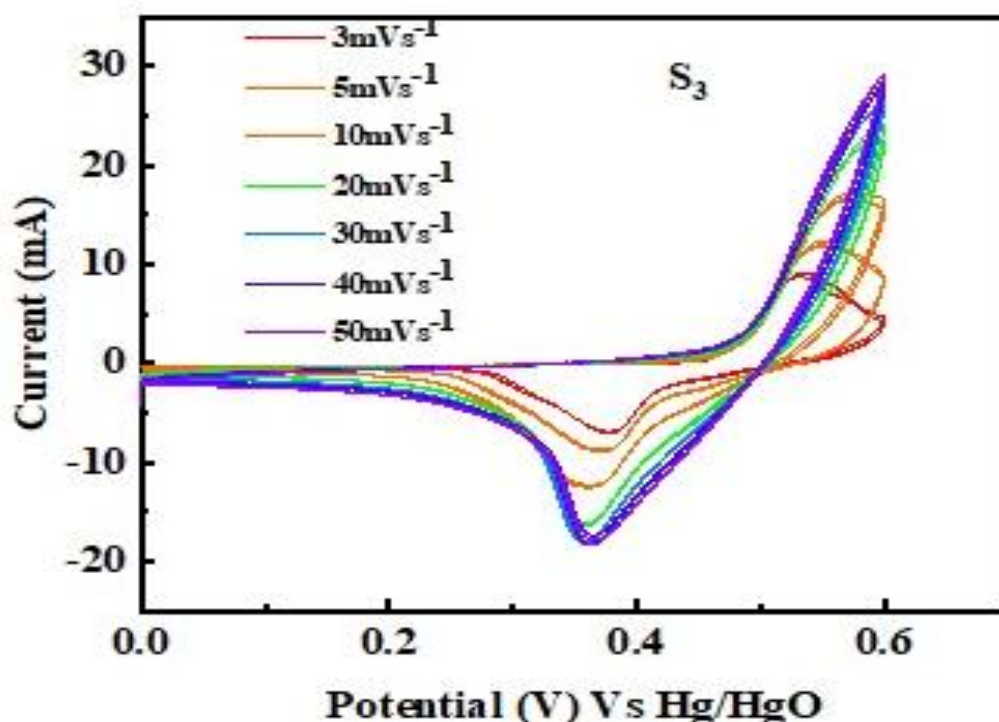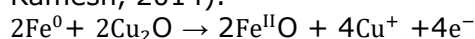$2Fe^0 + 2Cu_2O \rightarrow 2Fe^{II}O + 4Cu^+ + 4e^-$

Figure 8: C.V curves of Manganese Copper ferrites ($Mn_xCu_{1-x} Fe_2O_4$ at x=0.50)

Conclusion

Mn substituted Copper ferrites $Mn_xCu_{1-x} Fe_2O_4$ at x = 0.00, 0.33, 0.67, 1.00 were successfully synthesized from metal nitrates and citric acid by sol-gel method. This study shows the effects of Mn substitution on structural, magnetic and electric properties of copper ferrites. From XRD diffraction, crystalline nature and spinel structure of sample is revealed. Lattice parameter was found to be increased from 8.369 Å to 8.529 Å, it's due to

the substitution of Mn^{+2} having larger ionic radii 0.082nm then Fe^{+3} 0.064 nm. Distance between cations, anions and bond-angles confirmed the presence of tetrahedral and octahedral sites. Fourier transform infrared spectroscopy (FTIR), shows the fluctuating of absorption peaks of octahedral sites and stretching from 1422 cm^{-1} to 1434 cm^{-1}. This may be due to abrupt decrease in bond length with Mn doping copper ferrites as compared to pure copper ferrites. Above 3000 cm^{-1} peaks of O-H functional group was appeared due to absorption of moisture molecules. SEM shows the morphology of the samples. From SEM, grains also showed porous spherical surface of prescribe synthesized samples. Mean grain size calculated by line intercept method was 221 nm for pure copper ferrites and 286 nm, 324 nm and 373 nm for Mn substituted ferrites. The coercivity (Hc) of all prepared the sample is in the range or in few hundreds, which is one of the essential conditions for all electromagnetic materials and suggest these materials ideal for microwave instruments, security, switching and multiple sensing applications. Cyclic voltammetry calculations show efficient electrochemical properties with high specific capacitance that means the prepared sample is best for data storage devices such as lithium ion batteries (LIBs).

Reference

Ahmad, M., Shahid, M., Alanazi, Y. M., ur Rehman, A., Asif, M., & Dunnill, C. W. (2022). Lithium ferrite (Li0. 5Fe2. 5O4): synthesis, structural, morphological and magnetic evaluation for storage devices. *Journal of Materials Research and Technology, 18*, 3386-3395.

Ahmed, M., Okasha, N., Oaf, M., & Kershi, R. (2007). The role of Mg substitution on the microstructure and magnetic properties of Ba Co Zn W-type hexagonal ferrites. *Journal of Magnetism and Magnetic Materials, 314*(2), 128-134.

Akhtar, M. N., Ali, K., Umer, A., Ahmad, T., & Khan, M. A. (2018). Structural elucidation, and morphological and magnetic behavior evaluations, of low-temperature sintered, Ce-doped, nanostructured garnet ferrites. *Materials Research Bulletin, 101*, 48-55.

Akhtar, M. N., Sulong, A., Ahmad, M., Khan, M. A., Ali, A., & Islam, M. (2016). Impacts of Gd–Ce on the structural, morphological and magnetic properties of garnet nanocrystalline ferrites synthesized via sol–gel route. *Journal of Alloys and Compounds, 660*, 486-495.

Anwar, A., Zulfiqar, S., Yousuf, M. A., Ragab, S. A., Khan, M. A., Shakir, I., & Warsi, M. F. (2020). Impact of rare earth Dy+ 3 cations on the various parameters of nanocrystalline nickel spinel ferrite. *Journal of Materials Research and Technology, 9*(3), 5313-5325.

Blomgren, G. E. (2016). The development and future of lithium ion batteries. *Journal of The Electrochemical Society, 164*(1), A5019.

Bruce, P. G., Freunberger, S. A., Hardwick, L. J., & Tarascon, J.-M. (2012). Li–O2 and Li–S batteries with high energy storage. *Nature materials, 11*(1), 19-29.

Castaldi, M., Quadri, L., Sangiorgio, V. A., Arnaudo, P., Muthukumaran, P., Bernelli Zazzera, F., . . . Mainini, L. (2021). Power generation systems for L-MOXIE: concept proposal and trade-off analysis. In *ASCEND 2021* (pp. 4186).

Cullity, B. D. (1956). *Elements of X-ray Diffraction*: Addison-Wesley Publishing.

Dar, M. A., Shah, J., Siddiqui, W., & Kotnala, R. (2012). Influence of synthesis approach on structural and magnetic properties of lithium ferrite nanoparticles. *Journal of Alloys and Compounds, 523*, 36-42.

Deng, N., Kang, W., Liu, Y., Ju, J., Wu, D., Li, L., . . . Cheng, B. (2016). A review on separators for lithiumsulfur battery: progress and prospects. *Journal of Power Sources, 331*, 132-155.

George, M., Nair, S. S., John, A. M., Joy, P., & Anantharaman, M. (2006). Structural, magnetic and electrical properties of the sol-gel prepared Li0. 5Fe2. 5O4 fine particles. *Journal of Physics D: Applied Physics, 39*(5), 900.

Javed, Z., Rasool, R. T., Alhummiany, H., Majeed, A., Gulbadan, S., Ashraf, G. A., . . . Arshad, M. (2024). Structural, morphological, dielectric, and spectral properties of Sr-Mg-Ho X-type magnetic nano materials suitable for microwave absorption application. *Vacuum*, 112965.

Kamat, P. V. (2019). Lithium-ion batteries and beyond: Celebrating the 2019 Nobel Prize in chemistry–a virtual issue. *ACS Energy Letters, 4*(11), 2757-2759.

Khoso, W. A., Haleem, N., Baig, M. A., & Jamal, Y. (2021). Synthesis, characterization and heavy metal removal efficiency of nickel ferrite nanoparticles (NFN's). *Scientific Reports, 11*(1), 3790.

Kim, T., Song, W., Son, D.-Y., Ono, L. K., & Qi, Y. (2019). Lithium-ion batteries: outlook on present, future, and hybridized technologies. *Journal of materials chemistry A, 7*(7), 2942-2964.

Kurian, M., & Kunjachan, C. (2014). Investigation of size dependency on lattice strain of nanoceria particles synthesised by wet chemical methods. *International Nano Letters, 4*, 73-80.

Kurmude, D., Barkule, R., Raut, A., Shengule, D., & Jadhav, K. (2014). X-ray diffraction and cation distribution studies in zinc-substituted nickel ferrite nanoparticles. *Journal of Superconductivity and Novel Magnetism, 27*, 547-553.

Lain, M. J., Brandon, J., & Kendrick, E. (2019). Design strategies for high power vs. high energy lithium ion cells. *Batteries, 5*(4), 64.

Li, G. (2017). SHANGHAITECH SEM WORKING PAPER SERIES No. 2018-008.

Li, S., Lan, L., Lu, L., Lu, Y., Li, S., Li, J., . . . Zhao, F. (2019). Cerium doped LiNi0. 5Mn1. 5O4 composite with improved high temperature performance as a cathode material for Li-ion batteries. *AIP Advances, 9*(2).

Lim, C.-S., Teoh, K., Liew, C.-W., & Ramesh, S. (2014). Electric double layer capacitor based on activated carbon electrode and biodegradable composite polymer electrolyte. *Ionics, 20*, 251-258.

Martinson, K. D., Beliaeva, A. D., Sakhno, D. D., Beliaeva, I. D., Belyak, V. E., Nianikova, G. G., . . . Popkov, V. I. (2022). Synthesis, Structure, and Antimicrobial Performance of NixZn1− xFe2O4 (x= 0, 0.3, 0.7, 1.0) Magnetic Powders toward E. coli, B. cereus, S. citreus, and C. tropicalis. *Water, 14*(3), 454.

Pachauri, N., Khodadadi, B., Althammer, M., Singh, A. V., Loukya, B., Datta, R., . . . Mewes, T. (2015). Study of structural and ferromagnetic resonance properties of spinel lithium ferrite (LiFe5O8) single crystals. *Journal of Applied Physics, 117*(23).

Reddy, B. C., Manjunatha, H., Vidya, Y., Sridhar, K., Pasha, U. M., Seenappa, L., . . . Sankarshan, B. (2021). Synthesis and characterization of multi functional nickel ferrite nano-particles for X-ray/gamma radiation shielding, display and antimicrobial applications. *Journal of Physics and Chemistry of Solids, 159*, 110260.

Srivastava, M., Ojha, A. K., Chaubey, S., Sharma, P. K., & Pandey, A. C. (2010). Influence of pH on structural morphology and magnetic properties of ordered phase cobalt doped lithium ferrites nanoparticles synthesized by sol–gel method. *Materials science and engineering: B, 175*(1), 14-21.

Subramanya, B., & Bhat, D. K. (2015). Novel eco-friendly synthesis of graphene directly from graphite using 2, 2, 6, 6-tetramethylpiperidine 1-oxyl and study of its electrochemical properties. *Journal of Power Sources, 275*, 90-98.

Tang, T., & Hou, Y. (2020). Chemical confinement and utility of lithium polysulfides in lithium sulfur batteries. *Small Methods, 4*(6), 1900001.

Tarascon, J.-M. (2010). Key challenges in future Li-battery research. *Philosophical Transactions of the Royal Society A: Mathematical, Physical and Engineering Sciences, 368*(1923), 3227-3241.

Thorvaldsen, A. (1997). The intercept method—2. Determination of spatial grain size. *Acta materialia, 45*(2), 595-600.

Vigneswari, T., & Raji, P. (2018). Structural, magnetic and optical properties of Al-substituted nickel ferrite nanoparticles. *International Journal of Materials Research, 109*(5), 413-421.

Waldron, R. (1955). Infrared spectra of ferrites. *Physical review, 99*(6), 1727.

Yan, Z., & Luo, J. (2017). Effects of CeZn co-substitution on structure, magnetic and microwave absorption properties of nickel ferrite nanoparticles. *Journal of Alloys and Compounds, 695*, 1185-1195.

Zeng, H., Tao, T., Wu, Y., Qi, W., Kuang, C., Zhou, S., & Chen, Y. (2014). Lithium ferrite (Li 0.5 Fe 2.5 O 4) nanoparticles as anodes for lithium ion batteries. *RSC advances, 4*(44), 23145-23148.

Zhang, R., & Fujimori, S. (2020). The role of transport electrification in global climate change mitigation scenarios. *Environmental Research Letters, 15*(3), 034019.